# Secondary effects in wide frequency range measurements of the pyroelectric coefficient of $Ba_{0.6}Sr_{0.4}TiO_3$ and $PbZr_{0.2}Ti_{0.8}O_3$ epitaxial layers

Trong Tong,[*] J. Karthik, Lane W. Martin, and David G. Cahill

*Department of Materials Science and Engineering and Materials Research Laboratory, University of Illinois, Urbana, Illinois 61801, USA*

We describe measurements of the pyroelectric coefficient of epitaxial layers of $Ba_{0.6}Sr_{0.4}TiO_3$ (BST) and $PbZr_{0.2}Ti_{0.8}O_3$ (PZT) using a modulated laser as the heat source in the frequency range 1 Hz to 10 MHz. The pyroelectric coefficient is also measured as a function of applied static electric field and for films grown on $SrTiO_3$, $DyScO_3$, and $GdScO_3$ substrates. The heat diffusion equation is solved in cylindrical coordinates for the temperature field in a multilayer sample heated by a Gaussian-shaped laser beam. The secondary contribution to the pyroelectric effect caused by piezoelectric effects and in-plane thermal expansion is revealed by the difference between the pyroelectric coefficients at high and low frequencies. The secondary pyroelectric effect has the same dependence on applied field as the pyroelectric coefficient. The magnitude of the secondary effect changes with heating frequency because of changing mechanical conditions, but the pyroelectric coefficient has no other frequency dependence between 1 Hz and 10 MHz. The secondary effect is approximately 15% and 20% of the total pyroelectric response for PZT and BST films, respectively.

## I. INTRODUCTION

Pyroelectricity describes the change in the polarization of a material with temperature. A principle application of pyroelectricity is in detectors of infrared radiation [1]. More recently, novel applications of pyroelectric materials have employed epitaxial layers and microfabricated devices to enable new functions, e.g., high frequency thermal-to-energy conversion [2,3]. The use of thin epitaxial layers enables engineering of the properties of the ferroelectric layers by varying epitaxial strain and composition [4–8]. The relative roles of intrinsic, extrinsic, and secondary effects are not well established [9–11]. Typically, the change in polarization with increasing temperature is attributed to increasing thermal disorder of electric dipoles. Using molecular dynamics studies, Peng and Cohen [12] recently showed that the origin of pyroelectricity of $LiNbO_3$ is the result of changes in atomic positions with temperature driven by anharmonicity of lattice vibrations.

A measurement of the pyroelectric coefficient $dP/dT$ is the sum of the primary pyroelectric coefficient (what would be measured if the sample could be held at constant strain) and the secondary pyroelectric coefficient, which arises from the fact that pyroelectric materials are also piezoelectric and thus thermal expansion (or, more specifically, thermal expansion mismatch between a substrate and thin film) gives rise to a shape change and corresponding stress that drives an additional change in the polarization with temperature [13–15]. Studies of the secondary pyroelectricity of bulk materials have been carried out by many researchers and have been reported to be both negligible [16] and highly significant [17–19] in different systems.

In the pyroelectric measurement of a thin film on a thick substrate, the film is free to expand in the thickness direction. However, in the in-plane direction, a film is constrained by its substrate. For the case in which a film is attached to a substrate and the bulk substrate temperature is fixed, the "planar-clamped" pyroelectric coefficient, $\Pi_1$, is described by (see eq. (8) of Ref. [14])

$$\Pi_1 = \Pi - \frac{2d_{31}\alpha_1}{s_{11} + s_{12}}. \tag{1}$$

Here $\Pi$ is the pyroelectric coefficient at constant stress, $d_{31}$ is the piezoelectric coefficient, $\alpha_1$ is the thermal expansion coefficient of the film, and $s_{11}$ and $s_{12}$ are components of the elastic compliance tensor of the film. If the substrate has the same temperature change as the film, the effective pyroelectric coefficient, $\Pi_2$ is (see eq. (9) of Ref. [14])

$$\Pi_2 = \Pi - \frac{2d_{31}(\alpha_1 - \alpha_{1s})}{s_{11} + s_{12}}. \tag{2}$$

Here, $\alpha_{1s}$ is the thermal expansion of the substrate. These relationships between the pyroelectric and piezoelectric effect [Eqs. (1) and (2)] are general and independent of the composition of the films.

In this paper, we describe a laser-based method to measure the pyroelectric coefficient of epitaxial layers over a wide frequency range. We apply this method to $Ba_{0.6}Sr_{0.4}TiO_3$ (BST) and $PbZr_{0.2}Ti_{0.8}O_3$ (PZT) epitaxial layers under varying static electric fields. The BST and PZT are selected as the subject of our study because deposition conditions and lattice structures are well established [20,21]. At high heating frequencies, the thermal diffusion distance is small compared to the lateral size of the capacitor structure we use to measure the pyroelectric coefficient; the measured pyroelectric coefficient is $\Pi_1$, described by Eq. (1). At low heating frequencies, the thermal diffusion distance is large compared to the lateral size of the capacitor, and the measured pyroelectric coefficient is $\Pi_2$, described by Eq. (2). Thus, by comparing measurements at high and low frequencies, we determine the contribution to the pyroelectric coefficient from in-plane thermal expansion $\Pi_2 - \Pi_1 = 2d_{31}\alpha_{1s}/(s_{11} + s_{12})$.

*trongvantong@gmail.com

## II. METHODS

Capacitor structures are fabricated from heterostructures of 20 nm $SrRuO_3$ (SRO)/150 nm BST or PZT/20 nm SRO grown on $SrTiO_3$ (STO), $DyScO_3$ (DSO), or $GdScO_3$ (GSO) substrates by pulsed-laser deposition and an MgO hard mask [21]. $SrRuO_3$, PZT, and BST layers were fabricated by pulsed-laser deposition employing a KrF excimer laser (wavelength = 248 nm). Ceramic SRO, $Pb_{1.1}Zr_{0.2}Ti_{0.8}O_3$, and BST targets were used for the growth. The SRO layer (thickness = 20 nm) was deposited at $630\,^{\circ}$C in an oxygen pressure of 100 mTorr with a laser fluence of $1.75\,J/cm^2$ at a laser repetition rate of 12 Hz. $PbZr_{0.2}Ti_{0.8}O_3$ and BST films (thickness = 150 nm) were grown from PZT and BST targets, respectively, with the same compositions. After growth, all the samples were cooled in 700 Torr pressure of oxygen to room temperature at 5 K/min. The thickness of the films is determined by deposition time and rate, which is calibrated for each material. The patterned SRO top electrode is fabricated using an MgO hard mask. $SrRuO_3$ is used as top and bottom electrodes because of its good metallic conductivity and lattice matching with perovskite substrates. These capacitor structures enable us to efficiently collect the pyroelectric current produced by heating the PZT or BST films with a modulated laser.

The radius of SRO top electrodes is 50 $\mu$m or 100 $\mu$m. Vanadium (V) films, $\approx$150 nm thick, are sputtered on top of the SRO top electrodes to produce an optically opaque layer that absorbs the incident laser power. Any metal that can efficiently absorb the laser power can be used as the top electrode. Here, we choose V because of its compatibility with the fabrication process. Thermal conductivities of each layer are measured by time domain thermoreflectance (TDTR). [22]. The thickness of the V layer is measured by picosecond acoustics [23].

Figure 1(a) shows a schematic diagram of the pyroelectric measurement. Our approach is similar to the laser intensity modulation method (LIMM) that was developed to measure the spatial distribution of polarization in ferroelectric materials [24]. A mode-locked Ti:sapphire laser operating at a wavelength of 785 nm is modulated in the frequency range of 1 Hz to 10 MHz by an electro-optic modulator (EOM) and focused on the surface of the V layer by a $5\times$ objective lens. The $1/e^2$ intensity radius of the focused laser spot is 10.3 $\mu$m. The laser power absorbed by the V layer produces an oscillating temperature within the ferroelectric film and substrate. To limit the steady-state temperature rise to less than 10 K, the average laser power is chosen to be 6 mW.

A lock-in amplifier synchronized to the laser modulation measures the current generated by charges that compensate for the change of polarization of the films in response to the temperature change. We use an audio frequency lock-in amplifier (SR830 - Stanford Research System) for a frequency range of 1 Hz to 100 kHz and a radio frequency lock-in amplifier (SR844) for a frequency range of 100 kHz to 10 MHz. To minimize the effects of device capacitance at high frequencies and increase the signal-to-noise ratio at low frequencies, the devices are connected directly to the current input of the lock-in amplifier (SR830) for frequencies from 1 Hz to 1 kHz. (The lock-in amplifier is set to current mode in which input impedance is 1 k$\Omega$.) For frequencies from 1 kHz to 100 kHz, the devices are connected to a preamplifier, which
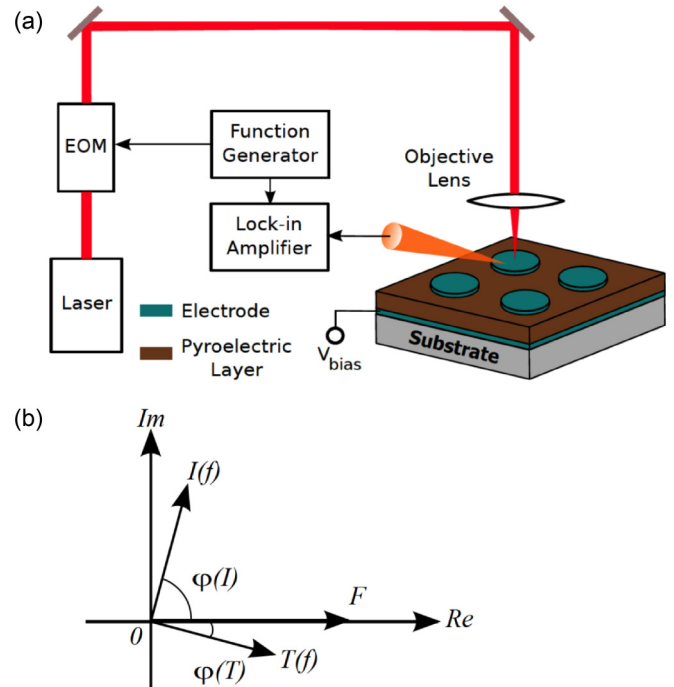


FIG. 1. (Color online) (a) Schematic description of the pyroelectric measurement. (b) Relative phases of the oscillating heat flux, $F$, temperature oscillations created by the heat flux, $T(f)$, and the measured ac current, $I(f)$. When nonpyroelectric currents are negligible in comparison with the pyroelectric current, the measured current leads the temperature change by 90°. The temperature change lags the heat flux by a phase angle, $\varphi(T)$, that depends on frequency. The phase angle of the current, $\varphi(I)$, is measured by the lock-in amplifier.

has input impedance of 50 $\Omega$. The output of the preamplifier is connected to the input of the SR830, which is set to the voltage mode with high input impedance. For frequencies from 100 kHz to 10 MHz, the devices are connected directly to the 50 $\Omega$ input of the SR844. To remove odd harmonics of frequencies that are not removed by the square wave mixer of the SR844, we use a programmable low-pass filter with an attenuation slope of 24 dB/octave. The cutoff frequency is set to be two times higher than the modulation frequency. By measuring the pyroelectric current using low input impedance (50 $\Omega$ or 1000 $\Omega$), we minimize effects of device capacitance, i.e., the RC time constant of the device and input, on the measurements at high frequencies. As shown below, device capacitance only affects the signal at frequencies higher than 3 MHz

Figure 1(b) shows a schematic representation of the relative phases between laser power, pyroelectric current, and temperature. The pyroelectric current leads the oscillating temperature by 90°, while the temperature lags behind the heat flux at a phase angle that depends on frequency. The phase angle of the pyroelectric current is measured by the lock-in amplifiers. However, at high frequencies the measured phase angle of the pyroelectric current is also affected by the electrical components. Hence, to accurately measure the phase of the pyroelectric current, we replace the sample with a photodiode and measure the current generated by
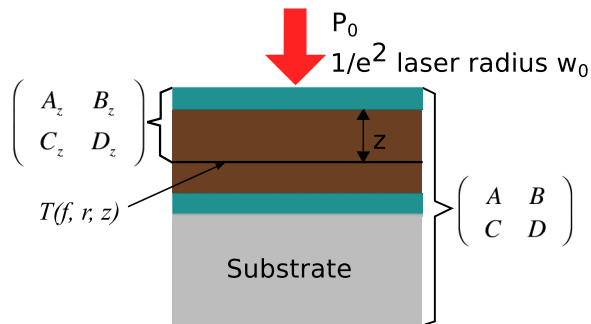
FIG. 2. (Color online) Heat transport model for the pyroelectric measurement. A Gaussian-shaped laser beam with a power $P_0$ and $1/e^2$ radius $w_0$ is absorbed at the V top layer. The temperature oscillation within the pyroelectric film is $T(f,r,z)$. $\begin{pmatrix} A & B \\ C & D \end{pmatrix}$ is the heat transport matrix for the entire sample, and $\begin{pmatrix} A_z & B_z \\ C_z & D_z \end{pmatrix}$ is the heat transport matrix for a part of the sample at a distance $z$ from the top layer.

the photodiode under an incident laser power with the same electronics. The phase angle of the photodiode is used to correct for the phase shifts introduced by the electronics. The corrected phase of the pyroelectric current is the difference between the measured phase of the pyroelectric current and the phase of the photodiode current. The rise time of the photodiode is $\sim 1$ ns.

The temperature oscillation, $T(f,r,z)$, within the pyroelectric layer is calculated by a multilayer thermal transport model in cylindrical coordinates (see Fig. 2). Here, $f$ is the modulation frequency, $r$ the radial coordinate, and $z$ the out-of-plane coordinate. The measured pyroelectric current is related to the temperature oscillation by

$$I(f) = 2\pi f \frac{1}{h} \frac{dP}{dT} \int_0^a \int_0^h T(f,r,z) 2\pi r \, dr \, dz, \quad (3)$$

where $dP/dT$ is the pyroelectric coefficient, $a$ is the radius of the top electrode of the capacitor, and $h$ is the thickness of the ferroelectric layer. The V layer is heated by a laser beam with a Gaussian distribution of intensity $F(r)$ and $1/e^2$ radius $w_0$,

$$F(r) = \frac{2P_0}{\pi w_0^2} \exp\left(-\frac{2r^2}{w_0^2}\right). \quad (4)$$

$P_0$ is the amplitude of the absorbed laser power. The Hankel transform of $F(r)$ is

$$F(k) = \frac{P_0}{2\pi} \exp\left(-\frac{k^2 w_0^2}{8}\right). \quad (5)$$

To solve for the temperature field $T(f,r,z)$ in the PZT or BST films, we apply a similar method, as described in Refs. [22,25]. In the frequency domain, a multilayer sample is represented by a heat transport matrix, which is a multiplication of matrices of individual layers,

$$M = M_N M_{N-1} \cdots M_1 = \begin{pmatrix} A & B \\ C & D \end{pmatrix}. \quad (6)$$

The individual matrix for each layer, $M_j$ ($j = 1, N$) is calculated as

$$M_j = \begin{pmatrix} \cosh(q_j d_j) & -\frac{1}{\Lambda_j q_j} \sinh(q_j d_j) \\ -\Lambda_j q_j \sinh(q_j d_j) & \cosh(q_j d_j) \end{pmatrix}. \quad (7)$$

Here, $d_j$ is the layer thickness, $\Lambda_j$ is the thermal conductivity, $q_j = \sqrt{k^2 + i\omega C_j / \Lambda_j}$, and $C_j$ is the volumetric heat capacity.

The temperature change at the V surface, $T_V(k)$, is related to the heat flux created by a laser, $F(k)$ by (see eq. (5) of Ref. [25])

$$T_V(k) = -\frac{D}{C} F(k), \quad (8)$$

where $D$, $C$ are the matrix elements from Eq. (6) for the entire sample, which includes V/SRO/PZT (or BST)/SRO/substrate. The temperature change at a distance $z$ from the SRO/BST or PZT interface, $T(k)$ in $k$ space, is related to $T_V(k)$ and $F(k)$ by

$$T(k) = A_z T_V(k) + B_z F(k) = \left(-A_z \frac{D}{C} + B_z\right) F(k), \quad (9)$$

where $A_z$, $B_z$ are the matrix elements as a function of $z$ for a part of the samples, which includes V, SRO, and a part of PZT or BST films at a distance $z$ from the SRO/PZT or SRO/BST interface. Combining with Eq. (5), the final solution for $T(f, r, z)$ in real space is the inverse transform of $T(k)$,

$$T(f,r,z) = \frac{P_0}{2\pi} \int_0^\infty \left(-A_z \frac{D}{C} + B_z\right) k J_0(kr)$$
$$\times \exp\left(-\frac{k^2 w_0^2}{8}\right) dk \quad (10)$$

Here, $J_0(kr)$ is the zero-order Bessel function.

### III. RESULTS

Figure 3 compares the experimental data and model calculation for the amplitude and phase of the pyroelectric current relative to the heat flux. In this version of the model, the pyroelectric coefficient is fixed at a value that is the best fit to the data at high frequencies. To understand how the heat flux is transported to the substrate, we compare the thermal penetration in the substrate, $d = \sqrt{\Lambda/\pi f C}$ to the laser spot size $w_0$. At low frequencies ($f < 1$ kHz), $d > w_0$ and heat spreads both laterally and perpendicular to the substrate surface. In the low frequency limit, the temperature change is in phase with the heat flux and scales with $1/\Lambda_{\text{sub}}$, where $\Lambda_{\text{sub}}$ is the thermal conductivity of the substrate. In this low frequency limit, the amplitude of the pyroelectric current is proportional to $\omega$, the temperature is in phase with the heat flux, and the phase of the pyroelectric current leads the heat flux by $90°$. In the high frequency limit ($f > 3$ MHz), $d < w_0$ and heat transport is approximately one-dimensional, normal to the surface of the sample, and the temperature change is mainly determined by the thermal properties of the films (BST or PZT).

At high frequencies ($f > 3$ MHz), the capacitive reactance of the device and cables are comparable to the $R = 50$ Ω input impedance of the lock-in amplifier used in the pyroelectric measurement. Therefore, the signal is suppressed by a factor

FIG. 4. Sensitivity of the calculated amplitude of the temperature oscillations, see Eq. (11), as a function of selected parameters in the thermal model as a function of heater frequency for a PZT film on a DSO substrate. The radius of the top contact is 50 $\mu$m. Sensitivity to the laser power is unity.
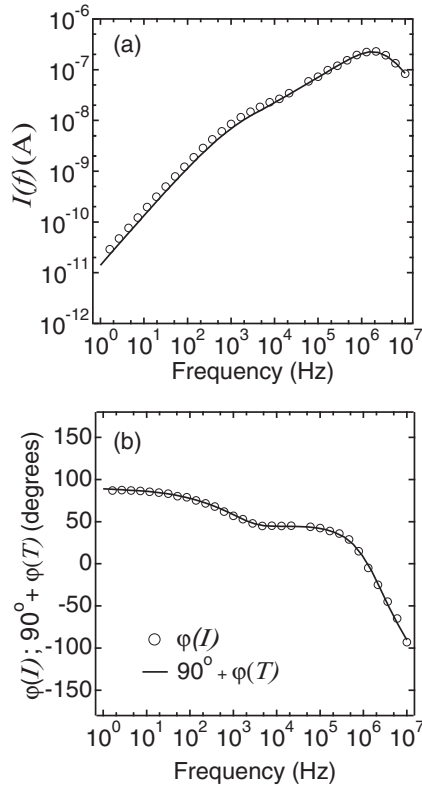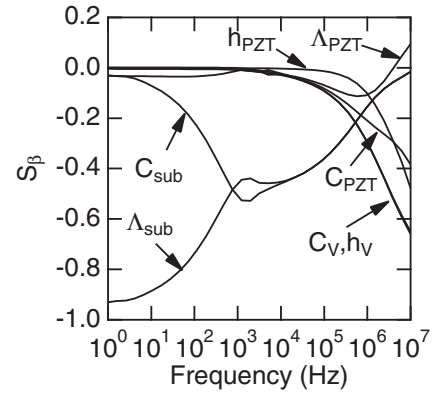
FIG. 3. (a) Frequency dependence of the amplitude of the pyroelectric current. Measured data are shown as open circles, and the solid line is the model calculations for a fixed value of the pyroelectric coefficient. (b) The measured phase angle of the current (open circles), $\varphi(I)$, and the phase angle of the pyroelectric current (solid line) calculated from the phase angle of the temperature, $90° + \varphi(T)$ for the BST/STO sample at zero bias voltage. The good match between the measured and calculated phase supports our assertion that nonpyroelectric currents are negligible in these experiments.

$1/(iRC\omega + 1)$, where $C$ is the effective capacitance of the device and cables. We adjust $C$ to have the best fit at high frequencies and find values of $C$ in range of 300–400 pF. For our measurement, capacitances of the devices is on the order of 100 pF and the total BNC cable length is $\sim$2.3 m. Since a typical BNC RG-58 cable has a capacitance of $\sim$100 pF/m, our fitting data of $C$ are on the order of the total equivalent capacitance of the circuit.

At intermediate frequencies (1 kHz $< f <$ 3 MHz), the temperature change is proportional to $1/\sqrt{i\omega\Lambda_{\mathrm{sub}}C_{\mathrm{sub}}}$, which results in an $\approx$45° difference between the pyroelectric current and the heat flux. The heat flux and amplitude of the pyroelectric current therefore scales with $1/\sqrt{\omega}$.

To evaluate the accuracy of measurement due to the propagation of errors from the values of the material properties, we define the sensitivity of the temperature response to each parameter in the thermal model by

$$S_\beta = \frac{\partial \ln T}{\partial \ln \beta}, \tag{11}$$

where $\beta$ is one of the parameters in the thermal model, i.e., thermal conductivity $\Lambda$, heat capacity $C$, or thickness $h$ of each layer. In Fig. 4, we plot the sensitivity of the temperature

calculation to the most important input parameters in the thermal model as a function of frequency. At low frequencies, the calculation is mostly sensitive to $\Lambda_{\mathrm{sub}}$, while at high frequencies the heat capacity and thickness of V and PZT are the most important parameters. At intermediate frequencies, the thermal effusivity of the substrate, $e_{\mathrm{sub}} = \sqrt{\Lambda_{\mathrm{sub}}C_{\mathrm{sub}}}$, is the most important parameter.

At low frequencies the measured current is higher than predicted by the model when using a pyroelectric coefficient fit to the high frequency data. If instead we adjust the pyroelectric coefficient to fit the experimental data to the model calculation at each frequency, we find $dP/dT \approx -230$ $\mu$C m$^{-2}$ K$^{-1}$ for $f < 1$ kHz and $dP/dT \approx -170$ $\mu$C m$^{-2}$ K$^{-1}$ for $f > 10$ kHz, see Fig. 5(a).

The apparent frequency dependence of $dP/dT$ is explained by the secondary contribution to the total pyroelectric current due to the combination of the piezoelectric effect and the thermal expansion of the film and substrate. At low frequency, the thermal penetration depth is large compared to the radius of the device, and the film expands or contracts with the substrate in the plane of the film. As a result, an additional current is generated by the polarization change that arises via the piezoelectric effect. At high frequency, the lateral dimensions of the film do not change because the film is clamped to the substrate, and the near surface layer of the substrate cannot expand laterally. Therefore, at high frequency, the contribution to the secondary pyroelectric coefficient from the lateral thermal expansion is zero. The difference between the pyroelectric coefficient at low and high frequencies can be calculated by subtracting Eq. (2) and (1),

$$\Delta\Pi = \Pi_2 - \Pi_1 = \frac{2d_{31}\alpha_{1s}}{s_{11} + s_{12}}. \tag{12}$$

Typically, $d_{31}$ is negative, which is consistent with our result ($\Delta\Pi < 0$).

The change in the pyroelectric coefficient is centered at a frequency of approximately 3 kHz. This transition frequency is independent of the laser spot size: we repeated the measurement with $1/e^2$ radii of the laser spot sizes between 2.5 and 25 $\mu$m and observed no change of the transition frequency.
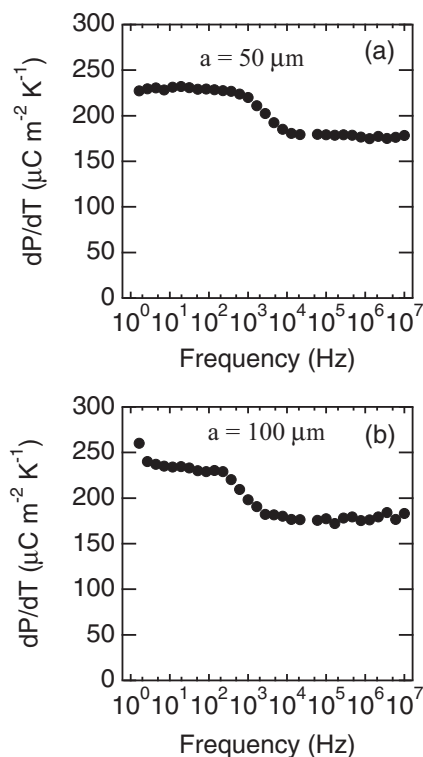
FIG. 5. Frequency dependence of the pyroelectric coefficient of the $Ba_{0.6}Sr_{0.4}TiO_3$ layer grown on a $SrTiO_3$ substrate. The radius of the top contact of the devices is (a) 50 $\mu$m and (b) 100 $\mu$m.

The transition frequency *does* depend on the radius of the top contact. For devices with a top contact that is a factor of two larger (radius of 100 $\mu$m), the transition frequency shifts to $\approx 700$ Hz [see Fig. 5(b)]; i.e., the transition frequency scales inversely with the square of the radius of the top contact as expected if the transition frequency is determined by the condition that the thermal penetration depth is comparable to the radius of the top electrode.

Our complete set of data for the pyroelectric coefficient of PZT and BST films on different substrates (DSO − DSO, GSO − GSO) under dc bias voltages at low (20 Hz) and high frequency (20 kHz) are summarized in Fig. 6. To apply a bias voltage to the films, we put the devices in series with the input impedance of the lock-in amplifier. One terminal of the voltage source is connected to the top electrode, and the other terminal is connected to ground potential. Because of the high resistance of the PZT or BST films (>1 M$\Omega$), the bias voltage is dropped completely across the films.

We observe hysteresis in the pyroelectric coefficients that resembles the polarization measurements. For the PZT samples [Figs. 6(a), 6(b)], the rectangularlike hysteresis loop is explained by the fact that the films are polarized either up or down with a well-defined coercivity. At the coercive voltages, the pyroelectric coefficient changes sign in response to the change in polarization between these two states.

By contrast, for BST films the pyroelectric coefficient depends on the applied field [Figs. 6(c), 6(d)]. Since the hysteresis loops are narrow, BST is better described as a relaxor ferroelectric [26–30], which typically has a broad ferroelectric transition [27] and nanoscale polar regions [28]. For an ideal
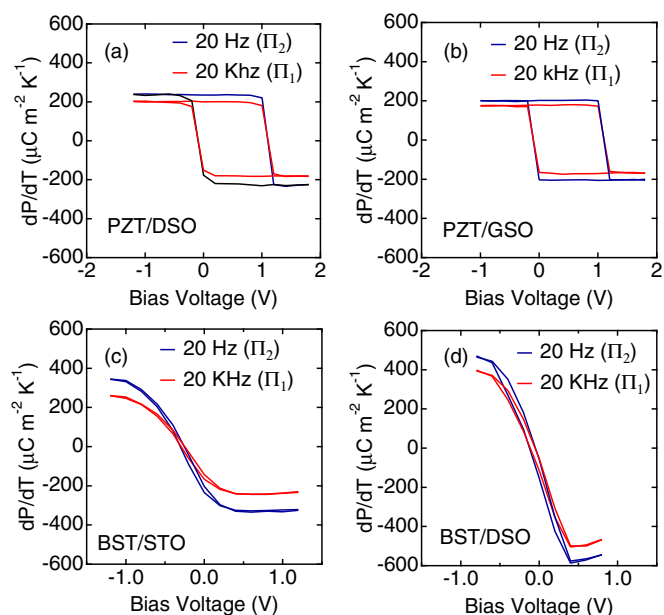


FIG. 6. (Color online) Hysteresis of the pyroelectric coefficient of PZT and BST films measured at 20 Hz and 20 kHz at room temperature. The *x* axis of each plot is the dc bias voltage that is applied to the capacitors. The time between changes in the bias voltage is ∼30 s, and the increment between values of the bias voltate is 0.2 V.

relaxor ferroelectric with randomly oriented nanodomains, the pyroelectric coefficient is zero at zero field and increases with increasing field because of increasing alignment of the nanodomains under an applied field. Our samples are not ideal, however, because the pyroelectric coefficient does not vanish at zero field but is instead shifted by a small amount toward negative bias voltage. $dP/dT$ eventually saturates at high field when all nanodomains are oriented in the field direction.

Figure 7 shows the electric field dependence of the secondary pyroelectric coefficient, i.e., the difference between low and high frequency measurements of the total pyroelectric coefficient. Using Eq. (12), we calculate the inverse piezoelectric constant $d_{31}$; $d_{31}$ determined by this approach is of the same order of magnitude with reported values for PZT films [31,32]. We observe that $d_{31}$ shows the same behavior as the pyroelectric coefficients.

The magnitude of the secondary pyroelectric coefficient provides insight about the origin of the pyroelectric effect in these samples. The secondary pyroelectric effect has been theoretically studied for epitaxial layers [14,15,33]. The secondary contribution for PZT was estimated to be approximately 10% of the total response by Karthik *et al.* [33] using Eq. (2) and reported a value of $d_{31}^{f}$. However, using a thermodynamic model for a polydomain PZT thin films, Karthik *et al.* in a later work [15] predicted a secondary pyroelectric contribution as high as 50% of the total response when taking into account the strain dependence of the polarization and the strain dependence of the volume fraction of domains oriented normal to the film. Furthermore, the thermodynamic model predicts that the secondary effect is only weakly dependent on the fraction of out-of-plane oriented
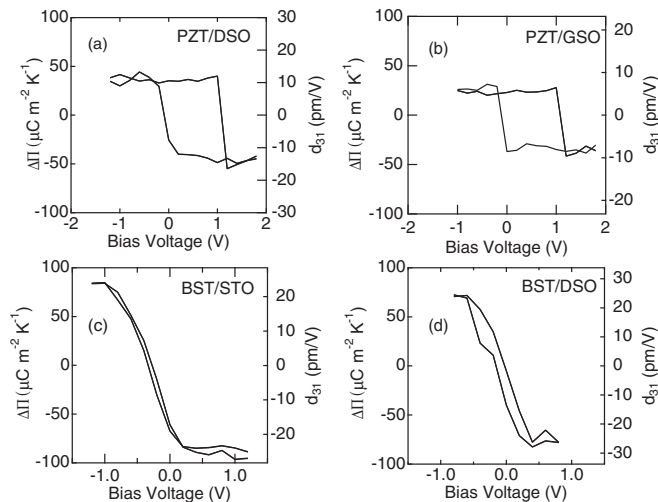
FIG. 7. Secondary pyroelectric coefficient of PZT and BST films due to the thermal expansion mismatch between the film and substrate as a function of the bias voltage. The right-hand axis of each plot is the corresponding converse piezoelectric coefficient $d_{31}$, calculated based on Eq. (12).

domains ($c$ domains). Zook and Liu's [14] calculation can be applied to both monodomain and polydomain samples because strain dependence of the polarization and the volume fraction of domain are both reflected in the piezoelectric coefficient $d_{31}^f$. Our result shows that the secondary contribution due to the in-plane thermal expansion of the substrate is less than 15% for the PZT films and 20% for the BST films. In addition, the secondary coefficient is approximately the same for PZT films on DSO and GSO substrates.

We used piezoresponse force microscopy (PFM) to characterize the domain structure of PZT and BST films. The $c$ domains fraction of the PZT film on DSO and GSO is ∼92% and 75%, respectively, while the BST films show no domain structure. These results are consistent with previous studies on PZT epitaxial layers [15] and BST films [28]. The thermodynamic model predicts the total pyroelectric coefficient increases with decreasing fraction of the $c$ domain [33]. However, our data show insignificant differences between the total pyroelectric coefficient for the PZT films on the DSO and GSO substrate. This could arise from domain wall pinning resulting in a smaller extrinsic contribution, which largely depends on the strain and domain fraction [15]. Moreover, the wide range frequency data show no frequency dependence of the pyroelectric coefficient up to 10 MHz. This result suggests to us that domain walls are pinned at all frequencies. Recently, Botea *et al.* [34] reported a pyroelectric coefficient (∼$1.9 \times 10^{-3}$ Cm$^{-2}$ K$^{-1}$, about 10 times higher that our measured values) of PZT epitaxial layers grown on STO substrates. The 90° ferroelectric domains and the compressive misfit strain are suggested to be causes for this giant value. More research is needed to directly study the contribution of the domain wall movement to the overall pyroelectric coefficient.

## IV. CONCLUSION

In conclusion, we describe a wide frequency-range method to measure the pyroelectric coefficient of epitaxial thin films of pyroelectric materials with high accuracy. A multilayer thermal transport model is developed to solve the temperature oscillation created by the laser power. By analyzing the difference of the pyroelectric coefficients at high and low frequency, which is caused by the clamped effect of the films on the substrates, the secondary contribution of the pyroelectric coefficient is measured. The secondary contribution to the pyroelectric coefficient of the PZT and BST films are measured to be ∼15% and 20%, respectively. The piezoelectric coefficient $d_{31}$ is calculated from the secondary effect. Our method enables studies of the secondary pyroelectric effect of clamped films directly and can be applied to studies of materials with potentially large pyroelectric and piezoelectric effect. For example, we speculate that the secondary effect could play a particularly important role in PZT films with composition near the morphotropic phase boundary.

[1] R. W. Whatmore, Rep. Prog. Phys. **49**, 1335 (1986).

[2] J. F. Scott, Science **315**, 954 (2007).

[3] Y. Y. Yang, W. W. Guo, K. C. K. Pradel, G. G. Zhu, Y. Y. Zhou, Y. Y. Zhang, Y. Y. Hu, L. L. Lin, and Z. L. Z. Wang, Nano Lett. **12**, 2833 (2012).

[4] M. Dawber and J. F. Scott, Rev. Mod. Phys. **77**, 1083 (2005).

[5] D. M. Kim, C. B. Eom, V. Nagarajan, J. Ouyang, R. Ramesh, V. Vaithyanathan, and D. G. Schlom, Appl. Phys. Lett. **88**, 142904 (2006).

[6] V. Nagarajan, S. Prasertchoung, T. Zhao, H. Zheng, J. Ouyang, R. Ramesh, W. Tian, X. Q. Pan, D. M. Kim, C. B. Eom, H. Kohlstedt, and R. Waser, Appl. Phys. Lett. **84**, 5225 (2004).

[7] N. Setter, D. Damjanovic, L. Eng, G. Fox, S. Gevorgian, S. Hong, A. Kingon, H. Kohlstedt, N. Y. Park, G. B. Stephenson,

I. Stolitchnov, A. K. Taganstev, D. V. Taylor, T. Yamada, and S. Streiffer, J. Appl. Phys. **100**, 051606 (2006).

[8] A. Sharma, Z. G. Ban, S. P. Alpay, and J. V. Mantese, Appl. Phys. Lett. **84**, 4959 (2004).

[9] A. Glass and M. Lines, Phys. Rev. B **13**, 180 (1976).

[10] R. T. Smith and F. S. Welsh, J. Appl. Phys. **42**, 2219 (1971).

[11] J. Mangin and A. Hadni, Phys. Rev. B **18**, 7139 (1978).

[12] Q. Peng and R. E. Cohen, Phys. Rev. B **83**, 220103 (2011).

[13] S. B. Lang, Phys. Rev. B **4**, 3603 (1971).

[14] J. D. Zook and S. T. Liu, J. Appl. Phys. **49**, 4604 (1978).

[15] J. Karthik, J. C. Agar, A. R. Damodaran, and L. W. Martin, Phys. Rev. Lett. **109**, 257602 (2012).

[16] Y. Tang, S. Zhang, Z. Shen, W. Jiang, J. Luo, R. Sahul, and T. R. Shrout, J. Appl. Phys. **114**, 084105 (2013).

[17] H. H. S. Chang and Z. Huang, Appl. Phys. Lett. **92**, 152903 (2008).

[18] K. H. Chew, F. G. Shin, B. Ploss, H. L. W. Chan, and C. L. Choy, J. Appl. Phys. **94**, 1134 (2003).

[19] Y. Yvry, V. Lyahovitskaya, I. Zon, I. Lubomirsky, E. Wachtel, and A. L. Roytburd, Appl. Phys. Lett. **90**, 172905 (2007).

[20] N. Izyumskaya, Y. Alivov, S. J. Cho, H. Morkoc, H. Lee, and Y. S. Kang, Crit. Rev. Solid State Mater. Sci. **32**, 111 (2007).

[21] J. Karthik, A. R. Damodaran, and L. W. Martin, Adv. Mater. **24**, 1610 (2012).

[22] D. Cahill, Rev. Sci. Instrum. **75**, 5119 (2004).

[23] W. S. Capinski, H. J. Maris, T. Ruf, M. Cardona, K. Ploog, and D. S. Katzer, Phys. Rev. B **59**, 8105 (1999).

[24] S. B. Lang and D. K. Das-Gupta, Ferroelectrics **60**, 23 (1984).

[25] A. Schmidt, M. Chiesa, X. Chen, and G. Chen, Rev. Sci. Instrum. **79**, 064902 (2008).

[26] C. Hubert, J. Levy, E. J. Cukauskas, and S. W. Kirchoefer, Phys. Rev. Lett. **85**, 1998 (2000).

[27] K. R. Carroll, J. M. Pond, D. B. Chrisey, J. S. Horwitz, R. E. Leuchtner, and K. S. Grabowski, Appl. Phys. Lett. **62**, 1845 (1993).

[28] D. A. Tenne, A. Soukiassian, M. H. Zhu, A. M. Clark, X. X. Xi, H. Choosuwan, Q. He, R. Guo, and A. S. Bhalla, Phys. Rev. B **67**, 012302 (2003).

[29] M. Tyunina and J. Levoska, Phys. Rev. B **70**, 132105 (2004).

[30] R. J. Zednik, P. C. McIntyre, J. D. Baniecki, M. Ishii, T. Shioga, and K. Kurihara, J. Appl. Phys. **101**, 066104 (2007).

[31] H. Kueppers, T. Leuerer, U. Schnakenberg, W. Mokwa, M. Hoffmann, T. Schneller, U. Boettger, and R. Waser, Sens. Actuators A **97-98**, 680 (2002).

[32] J. F. Shepard, F. Chu, I. Kanno, and S. Trolier-McKinstry, J. Appl. Phys. **85**, 6711 (1999).

[33] J. Karthik and L. W. Martin, Phys. Rev. B **84**, 024102 (2011).

[34] M. Botea, A. Iuga, and L. Pintilie, Appl. Phys. Lett. **103**, 232902 (2013).